Submitted to *J. Geophys. Res. Solid Earth*

Imaging strong lateral heterogeneities across the contiguous US using body-to-surface wave scattering

Chunquan Yu[1,2*], Jorge C. Castellanos[2], Zhongwen Zhan[2]

[1] *Department of Earth and Space Sciences, Southern University of Science and Technology, Shenzhen, Guangdong 518055, China*

[2] *Seismological Laboratory, California Institute of Technology, Pasadena, CA 91125, USA*

Corresponding author: Chunquan Yu (yucq@sustech.edu.cn)

Key points:

1. Body-to-surface wave scattering is used to illuminate strong lateral heterogeneities across the contiguous US.
2. The geographic distribution of strong scatterers across the contiguous US correlates well with major geological features.
3. Sources of body-to-surface scattering include topographic relief, near-surface velocity gradient, and Moho offset.

Abstract

Body-to-surface wave scattering, originated from strong lateral heterogeneity, has been observed and modeled for decades. Compared to body waves, scattered surface waves propagate along the Earth's surface with less energy loss and, thus, can be observed over a wider distance range. In this study, we utilize surface waves converted from teleseismic *SH* or *Sdiff* wave incidence to map strong lateral heterogeneities across the entire contiguous US. We apply array-based phase coherence analysis to broadband waveforms recorded by the USArray Transportable Array and other permanent/temporary networks to detect coherent signals that are associated with body-to-surface wave scattering. We then locate the source of the scattering by back-propagating the beamformed energy using both straight-ray and curved-ray approximations. Our results show that the distribution of scatterers correlates well with known geological features across the contiguous US. Topographic/bathymetric relief along the continental slope off the Pacific Border is the major source of scattering in the western US. On the other hand, sedimentary basins, especially their margins, are the dominant scatterers in the central US. Moho offsets, such as the one around the periphery of the Colorado Plateau, are also a strong contributor to scattering, but isolating their effect from that of other near-surface structures without any additional constraints can be complicated. Finally, we demonstrate the possibility of using scattered surface waves to constrain subsurface velocity structures, as complementary to conventional earthquake- or ambient-noise-based surface wave tomography.

1 Introduction

Seismic scattering originated from structural heterogeneity covers a wide range of scales within the Earth's interior. Conventionally, stochastic approaches are employed to study high-frequency scattering process from random heterogeneity (Sato et al., 2012). One typical example is the characterization of *P* and *S* coda waves from local and regional earthquakes (Aki, 1969). On the other hand, deterministic imaging of subsurface structures has long been undertaken using either backward or forward scattering. For example, in earthquake seismology, receiver functions rely on the forward *P*-to-*S* scattering to image seismic discontinuities in the crust and mantle (Langston, 1979). Seismic reflection surveys utilize backward reflected waves to characterize petroleum reservoirs in exploration seismology and the Earth's crust in controlled-source crustal seismology (Prodehl and Mooney, 2012; Sheriff and Geldart, 1995).

Unlike subhorizontal structures, strong lateral heterogeneity associated with near-vertical structure poses a significant challenge in deterministic scattered-wave imaging. In exploration seismology, complex structures can be imaged using densely distributed sources and receivers, in combination with sophisticated imaging or inversion techniques, such as reverse time migration or full-waveform inversion (Sheriff and Geldart, 1995; Virieux and Operto, 2009). However, such frameworks do not generally apply to earthquake seismology. The sparse distribution of earthquake sources and seismic stations greatly limits the detection ability of subsurface lateral heterogeneities, such as basin edges, fault zones, and Moho offsets, despite them having strong effects on seismic waveforms. Furthermore, many seismic imaging methods, such as conventional receiver functions, assume subhorizontal structures, which cannot readily be applied to image strong lateral heterogeneities.

Body-to-surface wave conversion is a special case of seismic scattering originated from strong lateral heterogeneity. Compared to body-to-body wave scattering, scattered surface waves propagate horizontally along the Earth's surface with less decay due to 2D geometric spreading and, thus, can be recorded over a wider distance range. Both Rayleigh and Love waves that are converted from body waves have been observed previously (e.g. Bannister et al., 1990; Furumura et al., 1998; Maeda et al., 2014). Moreover, if the delay time with respect to some reference phases can be measured, it is then possible to use the scattered surface waves to locate strong lateral heterogeneities. For example, Yu et al (2017a) analyzed teleseismic waveforms recorded by the Southern California Seismic Network and found that strong *SH*-to-Love wave scattering is associated with pronounced bathymetric relief and possible Moho offset in the Southern California Continental Borderland. Similarly, Buehler et al (2018) documented strong *S*-to-Rayleigh waves that are scattered at the western US continental margin.

The contiguous US is rich in structural heterogeneities both at the surface and in the underlying lithosphere. To first order, the contiguous US can be roughly divided into the western, central and eastern US (Figure 1). The western US has undergone a complex tectonic history since Neoproterozoic and is still actively deforming today (Dickinson, 2004). It is characterized by high topography and short-wavelength variations at the surface (Figure 1a). Geophysical evidence reveals thin crust and lithosphere, as well as significant lateral variations in seismic velocity (e.g. Burdick et al., 2017; Ekström, 2017; Schmandt and Lin, 2014; Shen and Ritzwoller, 2016). In contrast, the central US is mainly composed of stable terranes of Precambrian cores (Whitmeyer and Karlstrom, 2007). For most regions, the surface landscape is low and flat (Figure 1a), and the crust and lithosphere are thick and uniform. However, significant lateral variations in subsurface structure exist. For instance, both shallow crustal

85 velocity and Moho depth change abruptly across the northern margin of the Gulf of Mexico basin
86 (e.g. Schmandt and Lin, 2014; Shen and Ritzwoller, 2016). The eastern US has undergone two
87 complete cycles of supercontinent formation during the Grenville and Appalachian orogenesis,
88 and subsequent breakup of Rodinia and Pangea, respectively (Hatcher et al., 2010; McLelland et
89 al., 2010). At present, the most prominent topographic feature is the Appalachian Mountains
90 which consists of a system of fold and thrust belts in eastern North America (Figure 1a).

91 Building upon our previous study in Southern California, here we attempt to systematically
92 search for strong lateral heterogeneities across the entire contiguous US using body-to-surface
93 wave scattering. We first apply phase coherence analysis to extract coherent scattered energies
94 and use back-projection techniques to locate their sources. We then evaluate possible
95 contributions from various factors, such as topographic relief, sedimentary basins and Moho
96 offset, on the body-to-surface wave scattering. Finally, we demonstrate that scattered surface
97 waves can potentially be used for constraining subsurface structures.

98

99 2 Data and Methods

100 *2.1 Preliminary data processing*

101 We collect broadband waveform data from globally distributed events that are recorded by the
102 USArray Transportable Array. Stations from other regional networks, such as the
103 Southern/Northern California Seismic Network, and temporary arrays are also included to
104 densify the station spacing, especially in the western US (Figure 1b). The complete coverage of

seismic stations provides a unique opportunity to map strong lateral heterogeneities across the entire contiguous US.

For earthquake sources, we use both shallow and deep events with magnitude ≥ 6.0 that occurred during the deployment of USArray Transportable Array from 2004 to 2015. Event information is obtained from USGS National Earthquake Information Center. We limit the epicentral distances of the events to be within 40^o and 120^o since, for events with shorter epicentral distances, the surface wave trains may arrive too close to the time window of interest. When the epicentral distance is larger than about 100^o, the core-mantle boundary diffracted wave is used as the reference phase, whose amplitude may decrease rapidly as epicentral distance increases.

Our data preprocessing is similar to that of Yu et al. (2017a). We first rotate seismograms from vertical/north/east components into vertical/radial/tangential components based on source and receiver geometry. Here, we focus on tangential-component seismogram as it involves less body-wave phases and thus is less complicated than the other two components. The seismograms are then bandpass filtered between 0.02 and 0.1 Hz with a zero-phase, two-pass Butterworth filter. Events with complex source signatures are removed, and traces with low signal-to-noise ratio are discarded by visual inspection using the Crazyseismic software (Yu et al., 2017b). Afterwards, the waveforms are aligned, normalized by the maximum peaks of the observed *SH* or *Sdiff* phase, and cut using a time window of [-200, 600] s around the picked arrival time of the reference phase. The application of this preprocessing and quality control scheme resulted in 206 high-quality events that were then selected for further analyses (Figure 1c).

2.2 Observations of body-to-surface wave scattering across the contiguous US

Body-to-surface wave scattering is associated with strong lateral heterogeneity. Synthetic waveform modeling demonstrates that body-to-surface wave scattering can be well excited by either a topographic relief or a Moho offset (Yu et al., 2017a). Similarly, sharp horizontal contrasts in the elastic properties of the subsurface, such as basin edges, can also be a strong source of scattered energy (Figure 2). Body-to-surface wave scattering, including both *P*/*SV*-to-Rayleigh wave scattering and *SH*-to-Love wave scattering, has been observed in many locations around the world (e.g. Bannister et al., 1990; Buehler et al., 2018; Furumura et al., 1998; Maeda et al., 2014; Yu et al., 2017a).

As an example, Figure 3 shows seismic waveforms recorded in the western, central and eastern US by the USArray Transportable Array from three high-quality events occurred in the Kermadec-Fiji-Tonga subduction zones, respectively. These events are deep in focal depth as indicated by clear depth phase *sSH*, which arrives 200~250 s after the direct *SH* or *Sdiff* phase. The characteristics of signals in the time window between the *SH* and *sSH* phases, e.g. 50-150 s, are distinctly different among these three events: data recorded in the western US seems to have much higher "noise" level than that recorded in the eastern US, while that in the central US is somewhat in between (cf. Figures 3b, 3c and 3d). Power spectrum density analysis further verify such observation (Figure S1). Furthermore, there is a systematic increase in delay times of these "noise-like" signals (with respect to the reference *SH* phase) as epicentral distance increases (Figures 3b and 3c). As we look more closely into waveforms from a local subarray in the western and central US, the delays of the signals are more apparent (Figure 4). In the former case (Figures 4a and 4c), our previous study has verified that the delayed signals are Love waves scattered from teleseismic *SH* wave incidence (Yu et al., 2017a). In the latter case, the delay of signals does not seem to monotonically increase with epicentral distance (Figures 4b and 4d). In

the following sections, we will demonstrate that these signals are also scattered surface waves but propagate slightly off the great-arc circle.

2.3 Phase coherence analysis

To characterize the scattered signals, we employ the array-based phase coherence analysis technique implemented by Yu et al (2017a), which was originally described by Schimmel and Paulssen (1997). Phase coherence analysis is superior to conventional linear beamforming techniques in detecting weak but coherent signals as it relies on instantaneous phase. We systematically scan horizontal slowness from 0 to 40 s/^{o} and back azimuth from -45^{o} to 45^{o} relative to the theoretical back azimuth. In Figure 5, we show phase coherence measurements for the above two subarrays (Figure 4). In both cases, scattered waves propagate roughly at a slowness of ~30 s/^{o} (Figures 5a and 5b), which corresponds to an apparent velocity of ~3.7 km/s, consistent with surface wave velocity at a central frequency ~10 s. The horizontal propagation direction of the scattered waves deviates from that of the incident body waves (*SH* or *Sdiff*), at an angle about -4^{o} and -15^{o} for the two subarrays in the western and central US, respectively (Figures 5c and 5d). Thus, the body-to-surface wave scattering process is not necessarily confined in the great circle plane. Nevertheless, in most cases we analyzed, the directional deviation is not significant.

2.4 Back-projections

To map the geographical distribution of scatterers, we apply further data processing. For each event, we first estimate the source wavelet and then subtract and deconvolve it from each trace. Traces within a 2^o radius bin around each station (subarray) are stacked for back azimuth from -45^o to 45^o relative to the theoretical back azimuth, with a horizontal slowness determined by maximizing the coherence of scatters. We limit the horizontal slowness to be within 25 to 35 s/^{o} to avoid contamination from other phases and to stabilize the estimation, although in some locations the expected value may be outside this range. Subarrays with few traces (<20) are not processed in order to avoid strong spatial aliasing effect. The envelop functions of stacked traces are normalized, and incoherent signals are muted (Yu et al., 2017a). To minimize the contamination from scatters generated by other phases, we also mute signals starting with the arrival of *SS* for all epicentral distance, and the *ScS* for short epicentral distance (<75^o). We note that some scatters may escape detection but artifacts are minimized.

The next step of back-projection is to choose an accurate velocity model. In Southern California, the scattered surface wave has a dominant period ~10 s (Yu et al., 2017a). We find similar dominant periods for most events recorded by stations across the contiguous US. The scattered surface waves are mainly Love waves, since we focus on the transverse component and that the propagation direction of the scattered wave does not significantly deviate from the incident wave direction. Therefore, we use the 10 s Love group velocity as the background velocity model to perform the back-projection. There are a few existing high-resolution surface wave velocity models across the contiguous US (Ekström, 2017; e.g. Shen and Ritzwoller, 2016). Here, we calculate Love group velocities based on the USANT15 model (Ekström, 2017). The original USANT15 model provides Love phase velocities at different periods, and we use Rayleigh's formula to convert phase velocities to group velocities (Figure 6a). We acknowledge that the

193 exact surface-wave propagation velocity may slightly deviate from the background model, for
194 example due to different frequency content of the signal. However, since we use the envelop of
195 stacked traces for back-projection, the location uncertainties are acceptable considering the
196 spatial resolution of scatterers. In the region outside the contiguous US, there is no high-
197 resolution surface-wave velocity model available. For simplicity, we set a constant Love wave
198 group velocity of 3.1 km/s, which may result in mislocations of potential scatterers outside the
199 contiguous US. Here, however, we are mainly interested in locating scatterers within the
200 contiguous US.

201 Finally, we back-project the beamformed energy to map the geographical locations of scatterers.
202 We employ two different back-projection schemes using straight and curved rays, respectively.
203 For straight-ray back-projection, the envelop function of the stacked trace for each back azimuth
204 is mapped to geographic locations along a straight-ray trajectory. The distance to the center of
205 the sub array is determined by the arrival time of the scatter (relative to the incident *SH* or *Sdiff*
206 phase) and the background velocity model. Teleseismic *SH* wave arrival times are calculated
207 using the *ak135* reference Earth model (Kennett et al., 1995). As an example, Figures 6c and 6d
208 show the geographic distribution of travel times and back azimuths calculated using straight-ray
209 tracing from a hypothetical subarray center in the central US. Figure 7 shows straight-ray back-
210 projections of both phase coherence and amplitude for the two events recorded in western and
211 central US, respectively (Figures 3 and 4). Because the back-projection is applied to all
212 subarrays, the maximum values of phase coherence and amplitude at each grid point are used. A
213 minimum phase coherence of 0.5 is used to mute incoherent signals (Yu et al., 2017a).

214 It is well known that lateral variation in velocity can result in changes in the curvature of the
215 wavefield. To account for this effect, we apply curved-ray back-projection which applies the

Eikonal solver to trace surface-wave rays (Qin et al., 1992). We generate migration tables of travel times and back azimuths for gridded nodes (0.1^o by 0.1^o) for the entire contiguous US. Because of the focusing/defocusing effect, as well as the infinite frequency approximation of the Eikonal solution, ray geometry may change abruptly for nearby azimuths (Figure 6b). To stabilize the results, we apply a theoretical beamform at every node in the grid by taking the travel times of all neighboring nodes that are within a 2^o distance range and fitting the direction and slowness of a plane wave propagating through said subarray. This process allows us to retrieve the incidence angle of the plane waves generated at any scatter point in our study region as recorded by every 2^o radius subarray. Figures 6d and 6e show the geographic distribution of travel times and back azimuths calculated using curved-ray tracing. In regions with large velocity gradient, such as the Gulf of Mexico basin, the travel-time isochron is significantly different between straight-ray and curved-ray tracing (cf. Figures 6c and 6e).

3 Results

3.1 Directional sensitivity of scattering strength

The strength of body-to-surface wave scattering depends on not only the characters of scatterers but also the incident wave geometry. It appears that the scattering strength is strongest if the alignment of scatterers is perpendicular to the wave propagation direction. To visualize the directional sensitivity of scattering strength, we divide events into four groups based on their back azimuths, and stack back-projection results individually (Figure 8).

For events from the NW quadrant, strong scatterers are mainly located along the northern part of the Pacific Border and the offshore continental slope. Slightly weaker scatterers are detected around the Colorado Plateau, Rocky Mountains, and near the mid-continent rift zones (cf. Figures 1 and 8a). The scattering strength is strongest for events from the SW quadrant. Strong scatterers are widely distributed along the entire western coastal regions. However, they are weak or absent in the interior of the contiguous US, except for an isolated one in the southwestern part of Oklahoma in the central US (Figure 8c). For events from the SE quadrant, strong scatterers are located near the northern margin of the Gulf of Mexico basin in the southern part of the central US (cf. Figures 1 and 8d). Additional scatterers are seen round the Colorado Plateau, the Yellowstone region, Baja California, and the eastern coastal regions. The scattering strength is weakest for events from the NE quadrant, and scatterers are only sporadically detected in the northeastern part of the US (Figure 8b).

3.2 Strong scatterers across the contiguous US

To obtain an overall distribution of scatterers across the entire contiguous US, we merge the back-projection results from all directions (Figure 9). Overall, straight-ray and curved-ray back-projection results are consistent with each other. The first-order feature is that scatterers are both stronger and more widely distributed in the western US than in the eastern US, and that in the central US is in between. The result is consistent with data observations in Figure 3. The detailed back-projection results also depend on the choice of minimum phase coherence (cf. Figures 9 and S2) and, as such, we focus on the most robust features only.

In the western US, scatterers are widely distributed. Stronger scatterers are mainly located along the western coastal regions. This result is not surprising since this region is a plate boundary where there are strong lateral variations in both shallow and deep structures (cf. Figures 1 and 9). Interestingly, the strongest scatterer is located in the northern part of the Central Valley in California. Albeit weaker, scatterers are widely detected in other physiographic provinces, including the Cascade-Sierra Mountains, Basin and Ranges, the Colorado Plateau, and the Rocky Mountains. It appears that scatterers are much weaker in the interior of these physiographic provinces than at their margins. For example, there is almost no detection of scatterers in the interior of the northern Basin and Ranges.

In the central US, strong scatterers are mainly located in the southern part (Figure 9). The geographic distribution of scatterers correlates remarkably well with regions with strong lateral variations in short-period surface-wave velocity (cf. Figures 6a and 9). For example, the geometry of scatterers within Gulf of Mexico basin mimics the boundary of the low-velocity region. The NW-SE trending scatterer in Oklahoma correlates well with the low-velocity Anadarko Basin. In the northern part of central US, the mid-continental rift zone is a prominent scatterer, albeit with relatively weak scattering strength. The Superior Upland and nearby regions are also strong sources of scattering.

In the eastern US, scatterers are only sparsely distributed. Some isolated scatterers can be associated with the Appalachian Mountains and the continental slope. The weak detection of scatterers in the eastern US can result from either lack of strong lateral heterogeneities or lack of illuminating events from proper directions. We believe that the latter is the main reason because strong lateral variation in structures does exist, for example, along the continental slope or the

Appalachian front. However, there are no events that propagate roughly perpendicular to strike of these geological features (Figure 1c).

3.3 Difference between straight-ray and curved-ray back-projections

The detailed distribution of scatterers from straight-ray and curved-ray back-projections is different. It appears that scatterers imaged with curved-ray back-projection are more focused than the straight-ray back-projection in the interior of the contiguous US, where a high-resolution 2D velocity model is available (cf. Figures 9a and 9b). For example, in the curved-ray back-projection result, the mid-continent rift zone stands out more clearly and the periphery of the Colorado Plateau is well delineated (Figure 9b). Such difference indicates better location of scatterers using curved-ray back-projection and, in general, attests to the efficacy of the use of scattered waves as a tool to image sharp velocity contrasts. This last point is well-supported by the fact that, although the mid-continent rift is a prominent feature in gravity anomaly maps, traditional surface wave studies have had difficulty illuminating its fine-scale structure due to its narrow geometry (Figure 12). It is important to note that some weak scatterers with marginal coherence may not show up in the curved-ray back-projection result as it uses pre-calculated migration tables with a limited spatial resolution of 0.1^{o} (for the consideration of computational and storage costs).

Outside the contiguous US, the background velocity is fixed at a constant value (Figure 6a). As a result, neither straight-ray back-projection nor curved-ray back-projection can accurately locate scatterers. For example, the strong scatterer around Baja California is expected to be associated with the continental slope where bathymetric relief is significant (Figure 1a). However, the

straight-ray and curved-ray back-projections map that scatterer to the west and east of the continental slope, respectively (cf. Figures 1a and 9). In addition, the Eikonal ray tracing is likely to fail in regions with significant velocity gradient, such as the boundary of the Gulf of Mexico basin, where the curved-ray back-projection show smeared distribution of scatterers.

Henceforth, we will focus on the curved-ray back-projection result since it provides better locations of scatterers within the contiguous US, in which we are mostly interested.

4 Discussions

4.1 Sources of body-to-surface wave scattering

To better understand the sources of body-to-surface wave scattering, we explore three nominal factors that can potentially contribute to the body-to-surface wave scattering: topographic relief, lateral variation in near-surface velocity, and Moho offset. We compare them with back-projection results both in map view (Figure 10) and along selected profiles (Figure 11).

The most prominent source of scattering is topographic/bathymetric relief. In the Pacific Border region, the geographic distribution of scatterers show a nice spatial correlation with large gradient in bathymetry along the continental slope (cf. Figures 10a and 10b). The result is consistent with previous findings in this region (Buehler et al., 2018; Yu et al., 2017a). However, there is no detection of strong scatterers along the continental slope of Atlantic Plains, where topographic gradients are also significant. As mentioned earlier, this is likely due to lack of proper illumination of events from the SE direction. On the other hand, topographic relief is unable to explain many detected scatterers within the contiguous US. For example, there is

322 barely any prominent topographic relief in the central US, yet strong scatterers are clearly
323 observed (cf. Figures 10a and 10b).

324 Another source of scattering comes from lateral variation in velocity structure of the shallow
325 crust (velocity gradient), in which sedimentary basins play an important role. Since the
326 teleseismic incident *SH* wave and the scattered Love wave have a dominant period ~10 s, we use
327 10 s Love-wave group velocity to approximate the overall shallow crustal velocity. Locations of
328 scatterers near the northwestern margin of the Gulf of Mexico basin correlate well with a large
329 velocity gradient zone (cf. Figures 10a and 10c; profile AA' in Figure 11). The strong scatterer in
330 Oklahoma is interpreted to be associated with the Anakardo Basin, and the one in Arkansas is
331 likely associated with the Arkoma Basin and the Mississippi Embayment. In the northern part of
332 the Great Valley (Sacramento Basin) in California, low-velocity sediments must play a crucial
333 role in body-to-surface wave scattering as topographic relief alone is insufficient to explain the
334 observed strength of scatterers (Figure 10; profile BB' in Figure 11).

335 Deeper structures, such as Moho offset (or horizontal gradient of Moho depth), can also
336 contribute to body-to-surface wave scattering (Yu et al., 2017a). However, isolating the effect
337 from deeper structures is challenging as they are often collocated with shallow structural
338 heterogeneities. Due to smaller impedance contrast at the crust-mantle boundary than that at the
339 free surface, Moho offset typically plays a secondary role on the body-to-surface wave
340 scattering, unless significant amount of offset exists over a short horizontal distance. Here, we
341 document a few places that Moho offset might play an important role. Along profile BB' in
342 Figure 11, horizontal gradient of Moho depth is correlated with the scattering strength,
343 suggesting that it also contributes to body-to-surface wave scattering. In the profile CC' across
344 the Colorado Plateau (Figure 11), horizontal gradient of Moho depth fits the strength of scatterers

much better than topographic relief or near-surface velocity gradient. We hence suggest that Moho offset is the major source of body-to-surface wave scattering around the Colorado Plateau. For the case of the mid-continent rift zone, strong scatterers are correlated with gravity anomalies with a ~50 km offset in peak amplitude (Figure 12a). Here, however, it is complicated to attribute the large amount of scattering to a single structural heterogeneity. Detailed analysis of receiver functions across this province has revealed the existence of sharp crustal thickness differences and a complicated Moho structure which, together with the intermittent intra-crustal boundaries of the buried dense volcanic layers, have the potential of being a strong source of scattering (Chichester et al., 2018; Zhang et al., 2016). Moreover, the presence of thick low-velocity sediments that filled the basins created by the rift's extension can also be contributing the overall scattering strength (Foster et al., 2020; Green et al., 1989). Further work is required in order to accurately quantify the contribution from shallow and deep structures on body-to-surface wave scattering.

4.2 Scattering strength

The scattering strength depends on various factors, including the characters of scatterers and the incident wave geometry (Figure 8). In this study, we use the maximum amplitude measured at each subarray to represent the scattering strength of the scatterer. This is an approximation that assumes plane wave propagation and no amplitude-varying effect on the scattered surface wave. Attenuation can decrease the amplitude of the scattered surface wave when it propagates from the scatterer to the receiver. Focusing and defocusing effect can also change the amplitude. The amplitude of the reference incident wave used for normalization may be different at the location

of the scatterer and the receiver. Since we use teleseismic events that can be as far as 120^o, the amplitude of diffracted *SH* wave recorded at the subarray may be significantly smaller than that of the diffracted or direct *SH* at the scatterer's location. The amplitude may also be affected by SV-to-Rayleigh wave scattering since scattered surface wave can propagate off the great-arc circle. It is generally difficult to quantify these effects, and thus the measured amplitude ratio is only a rough estimation of the scattering strength.

4.3 Potentials for surface-wave tomography

Although scatterers are limited to certain locations, the scattered surface waves are widely recorded across the contiguous US. Therefore, it is possible to apply conventional surface-wave analysis to estimate their group and phase velocities, which can potentially be used for surface wave tomography. The frequency of scattered surface waves is relatively narrowband. The dominant period is between 10 and 20 s. Here, as a demonstration, we estimate the apparent velocity (reciprocal of the horizontal slowness) at each grid point by averaging valid measurements from all events. Only the most coherent slowness measurement is picked up for each subarray. The minimum phase coherence is set to 0.7 and the minimum scattering strength 0.05 (relative to the reference phase). Results within 1^o around each grid point are averaged.

Figure 13a shows the estimated apparent velocity of scattered surface waves across the contiguous US. The overall pattern resembles that of 20 s Love wave phase velocity obtained from ambient noise cross correlations (Figure 13b; Ekström, 2017). The correlation coefficient is high at 0.66 (Figure S3). Strictly speaking, our apparent velocity measurement cannot be directly compared with phase velocity at a fixed period. It is an average over a certain period range,

389 which may also vary among different events. Indeed, observed scattered surface wave in the
390 western US is relatively enriched in high-frequency content compared with that in the eastern US
391 (Figure S1). As a result, the overall apparent velocity is lower than and about the same as the 20
392 s Love wave phase velocity in the western and eastern US, respectively (cf. Figures 13a and
393 13b). Furthermore, our apparent velocity measurement is smoothed over a radius of ~1^{o}. In any
394 case, the overall similarity between Figure 13a and 13b demonstrates the potential of using
395 relatively short-period surface waves scattered from teleseismic body waves for constraining
396 subsurface structures, as complementary to conventional earthquake- or ambient-noise-based
397 surface wave tomography.

398

399 # 5 Conclusions

400 Body-to-surface wave scattering has been documented for several decades. Yet, its application to
401 deterministic structural imaging is scarce. Here, we take advantage of the dense coverage of the
402 USArray Transportable Array and other permanent/temporary networks to systematically map
403 strong lateral heterogeneities across the entire contiguous US by back-projection of scattered
404 surface waves converted from teleseismic *SH* or *Sdiff* wave incidence. Array-based phase
405 coherence analysis is employed to detect coherent signals that are associated with scattered
406 surface waves. Both straight-ray and curved-ray back-projections are used to locate scatterers.

407 Our results show that the distribution of scatterers correlates well with geological features across
408 the contiguous US. Potential scatterers include topographic relief, near-surface lateral velocity
409 gradient, and lateral variation in Moho depth. The contribution from topographic relief is most
410 evident along the continental slope off the Pacific Border. Margins of sedimentary basins are the

411 dominant scatterers in the central US. Moho offset is likely a major source of scatterers around
412 the Colorado Plateau. We also demonstrate that scattered surface waves can potentially be used
413 for surface-wave tomography in the future.

414

415 Acknowledgements

416 Seismic waveforms were retrieved from the Incorporated Research Institutions for Seismology
417 (IRIS) Data Management Center (https://ds.iris.edu/ds/nodes/dmc/, last accessed Aug 2020). This
418 research is supported by the NSF EarthScope grant 1829496 (Z. Zhan) and NSFC grant 41974043
419 (C. Yu).

420

References

Aki, K., 1969. Analysis of the seismic coda of local earthquakes as scattered waves. J. Geophys. Res. 74, 615–631.

Bannister, S., Husebye, E., Ruud, B., 1990. Teleseismic P coda analyzed by three-component and array techniques: deterministic location of topographic P-to-Rg scattering near the NORESS array. Bull. Seismol. Soc. Am. 80, 1969–1986.

Buehler, J.S., Mancinelli, N.J., Shearer, P.M., 2018. S-to-Rayleigh Wave Scattering From the Continental Margin Observed at USArray. Geophys. Res. Lett. 45, 4719–4724. https://doi.org/10.1029/2017GL076812

Burdick, S., Vernon, F.L., Martynov, V., Eakins, J., Cox, T., Tytell, J., Mulder, T., White, M.C., Astiz, L., Pavlis, G.L., Hilst, R.D. van der, 2017. Model Update May 2016: Upper- Mantle Heterogeneity beneath North America from Travel- Time Tomography with Global and USArray Data. Seismol. Res. Lett. 88, 319–325. https://doi.org/10.1785/0220160186

Chichester, B., Rychert, C., Harmon, N., Lee, S. van der, Frederiksen, A., Zhang, H., 2018. Seismic Imaging of the North American Midcontinent Rift Using S-to-P Receiver Functions. J. Geophys. Res. Solid Earth 123, 7791–7805. https://doi.org/10.1029/2018JB015771

Dickinson, W.R., 2004. Evolution of the North American cordillera. Annu Rev Earth Planet Sci 32, 13–45.

Ekström, G., 2017. Short-period surface-wave phase velocities across the conterminous United States. Phys. Earth Planet. Inter. 270, 168–175. https://doi.org/10.1016/j.pepi.2017.07.010

Foster, A., Darbyshire, F., Schaeffer, A., 2020. Anisotropic structure of the central North American Craton surrounding the Mid-Continent Rift: Evidence from Rayleigh waves. Precambrian Res. 105662.

Furumura, M., Kennett, B., Furumura, T., 1998. Anomalous surface waves associated with deep earthquakes, generated at an ocean ridge. Geophys. J. Int. 134, 663–676.

450 Green, A.G., Cannon, W., Milkereit, B., Hutchinson, D., Davidson, A., Behrendt, J.,
451 Spencer, C., Lee, M., Morel- á- LáHuissier, P., Agena, W., 1989. A “Glimpce “of
452 the Deep Crust Beneath the Great Lakes. Prop. Process. Earths Low. Crust 51,
453 65–80.
454 Hatcher, R.D., Tollo, R., Bartholomew, M., Hibbard, J., Karabinos, P., 2010. The
455 Appalachian orogen: A brief summary. Rodinia Pangea Lithotectonic Rec.
456 Appalach. Reg. Geol. Soc. Am. Mem. 206, 1–19.
457 Kennett, B., Engdahl, E., Buland, R., 1995. Constraints on seismic velocities in the
458 Earth from traveltimes. Geophys. J. Int. 122, 108–124.
459 Langston, C.A., 1979. Structure under Mount Rainier, Washington, inferred from
460 teleseismic body waves. J. Geophys. Res. Solid Earth 84, 4749–4762.
461 Maeda, T., Furumura, T., Obara, K., 2014. Scattering of teleseismic P-waves by the
462 Japan Trench: A significant effect of reverberation in the seawater column. Earth
463 Planet. Sci. Lett. 397, 101–110.
464 McLelland, J.M., Selleck, B.W., Bickford, M., Tollo, R., Bartholomew, M., Hibbard, J.,
465 Karabinos, P., 2010. Review of the Proterozoic evolution of the Grenville
466 Province, its Adirondack outlier, and the Mesoproterozoic inliers of the
467 Appalachians. Rodinia Pangea Lithotectonic Rec. Appalach. Reg. Geol. Soc.
468 Am. Mem. 206, 21–49.
469 Prodehl, C., Mooney, W.D., 2012. Exploring the Earth’s crust: history and results of
470 controlled-source seismology. Geological Society of America.
471 Qin, F., Luo, Y., Olsen, K.B., Cai, W., Schuster, G.T., 1992. Finite- difference solution of
472 the eikonal equation along expanding wavefronts. GEOPHYSICS 57, 478–487.
473 https://doi.org/10.1190/1.1443263
474 Sato, H., Fehler, M.C., Maeda, T., 2012. Seismic wave propagation and scattering in
475 the heterogeneous earth. Springer.
476 Schimmel, M., Paulssen, H., 1997. Noise reduction and detection of weak, coherent
477 signals through phase-weighted stacks. Geophys. J. Int. 130, 497–505.
478 Schmandt, B., Lin, F.-C., 2014. P and S wave tomography of the mantle beneath the
479 United States. Geophys. Res. Lett. 41, 2014GL061231.
480 https://doi.org/10.1002/2014GL061231

481 Shen, W., Ritzwoller, M.H., 2016. Crustal and uppermost mantle structure beneath the
482 United States. J. Geophys. Res. Solid Earth 121, 2016JB012887.
483 https://doi.org/10.1002/2016JB012887
484 Sheriff, R.E., Geldart, L.P., 1995. Exploration seismology. Cambridge university press.
485 Virieux, J., Operto, S., 2009. An overview of full-waveform inversion in exploration
486 geophysics. GEOPHYSICS 74, WCC1–WCC26.
487 https://doi.org/10.1190/1.3238367
488 Whitmeyer, S.J., Karlstrom, K.E., 2007. Tectonic model for the Proterozoic growth of
489 North America. Geosphere 3, 220–259.
490 Yu, C., Zhan, Z., Hauksson, E., Cochran, E., 2017a. Strong SH-to-Love wave scattering
491 off the Southern California Continental Borderland. Geophys. Res. Lett. 44,
492 10,208-10,215. https://doi.org/10.1002/2017GL075213
493 Yu, C., Zheng, Y., Shang, X., 2017b. Crazyseismic: A MATLAB GUI- based software
494 package for passive seismic data preprocessing. Seismol. Res. Lett. 88, 410–
495 415. https://doi.org/10.1785/0220160207
496 Zhang, H., Lee, S. van der, Wolin, E., Bollmann, T.A., Revenaugh, J., Wiens, D.A.,
497 Frederiksen, A.W., Darbyshire, F.A., Aleqabi, G.I., Wysession, M.E., Stein, S.,
498 Jurdy, D.M., 2016. Distinct crustal structure of the North American Midcontinent
499 Rift from P wave receiver functions. J. Geophys. Res. Solid Earth 121, 8136–
500 8153. https://doi.org/10.1002/2016JB013244
501
502

503 **Figures**

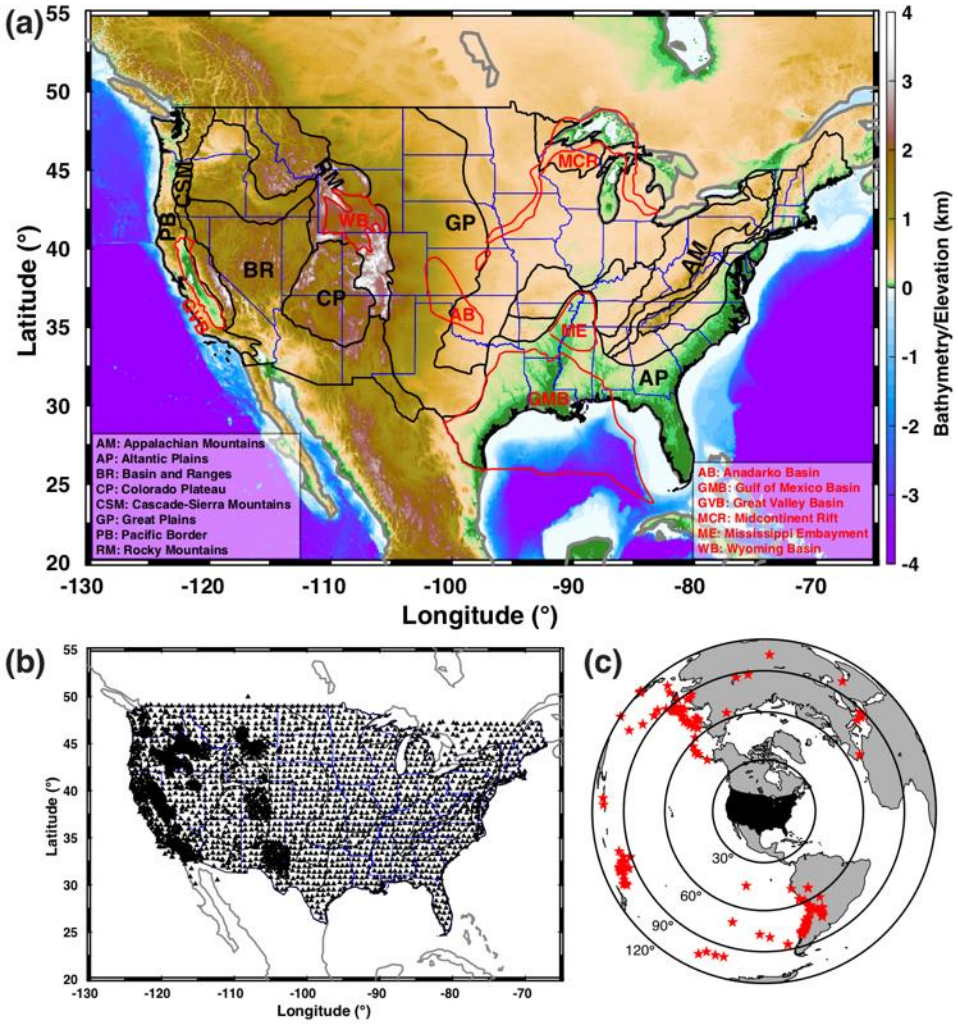

504

505 Figure 1 (a) Topographic map of the contiguous United States and adjacent areas. Black lines mark
506 boundaries of major physiographic provinces (Feneman, 1931). Red lines are contours of the
507 midcontinent rift zone and other sedimentary basins mentioned in the main text. Blue lines are
508 state borders. (b) Broadband seismic stations (solid triangles) used this study, including USArray
509 Transportable Array, US permanent network, Southern California Seismic Network, North
510 California Seismic Network, and other temporary deployments. (c) Distribution of 206 selected
511 earthquakes (red stars).

512

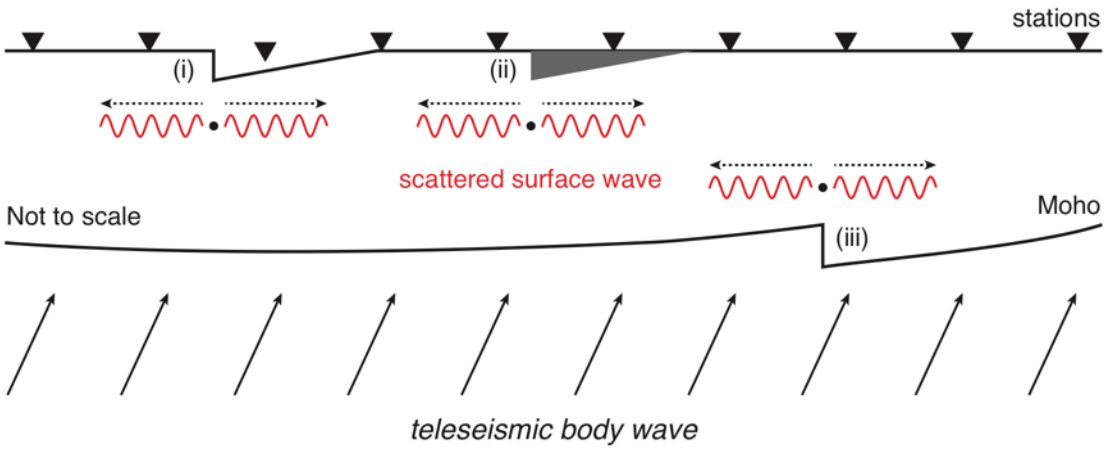

513

514 Figure 2 Schematic diagram showing body-to-surface wave scattering due to sharp lateral
515 heterogeneities, including (i) topographic relief, (ii) basin edge, and (iii) Moho offset.

516

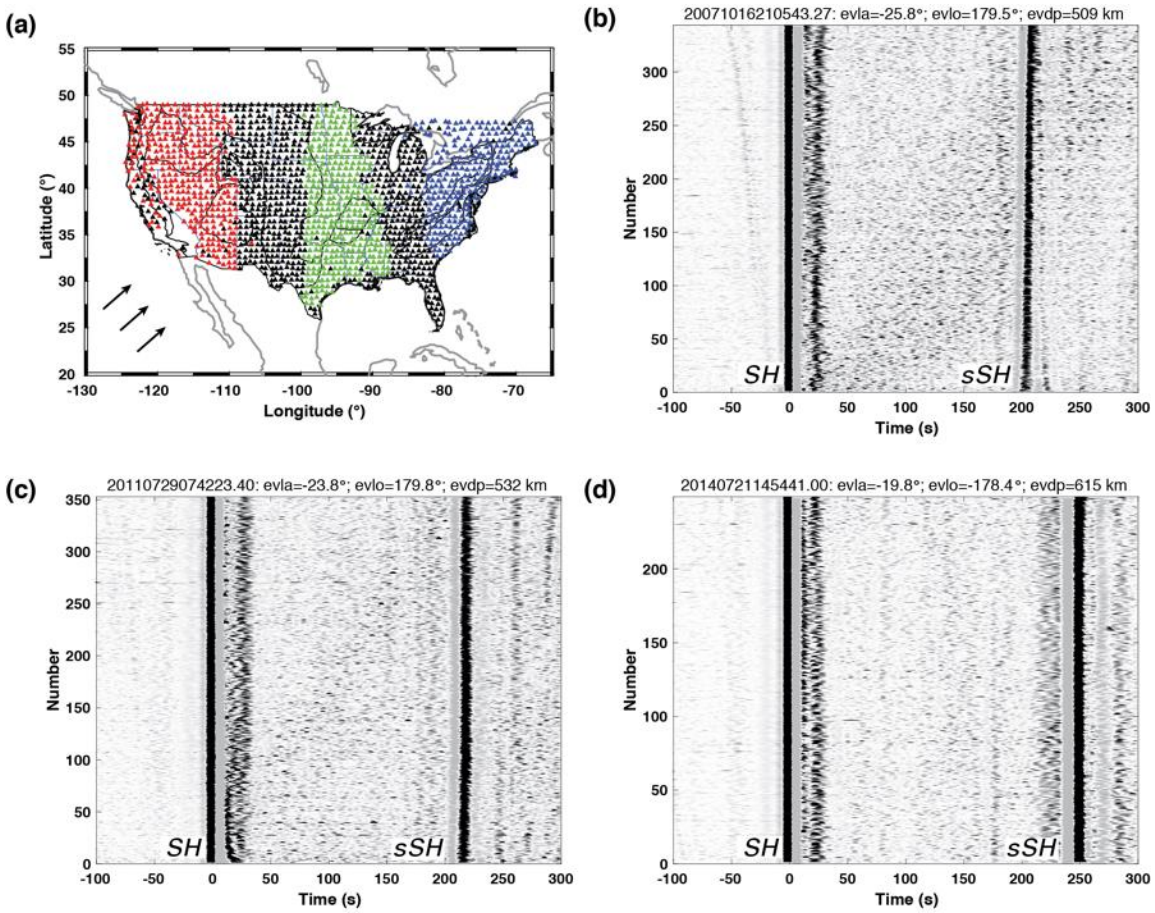

Figure 3 Teleseismic *SH* waveforms recorded at different locations across the contiguous US. (a) is the distribution of USArray transportable array. (b), (c) and (d) are waveforms from three deep events that occurred in the Tonga-Fiji-Kermadec subduction zone. Waveforms are aligned and normalized by the maximum peak of *SH* or *Sdiff* phase, and are sorted by epicentral distance. The depth phase *sSH* arrives >200 s later than the direct *SH* or *Sdiff* phase. Stations used in (b), (c) and (d) are shown as red, green and blue colors in (a), respectively.

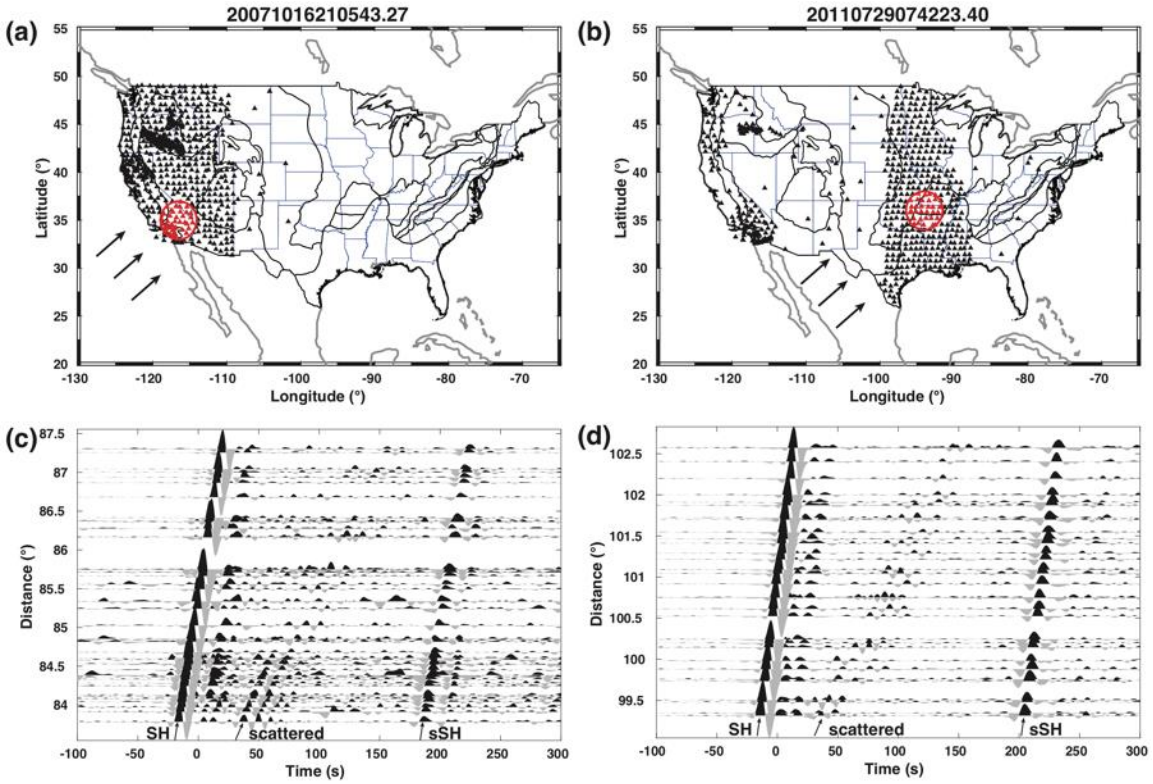

Figure 4 Observations of scattered surface waves from teleseismic *SH* incidences. (a) is the distribution of broadband seismic stations in the western United States for the same 2007 deep earthquake as in Figure 3b. (c) shows the recorded teleseismic waveforms (tangential component) for selected stations (red triangles in a) in a 2-degree radius circular area. Traces are sorted by epicentral distance. (b), (d) are the same as (a), (c), except for the 2011 deep earthquake shown in Figure 3c. Note that in both cases, scattered surface waves are clearly observed.

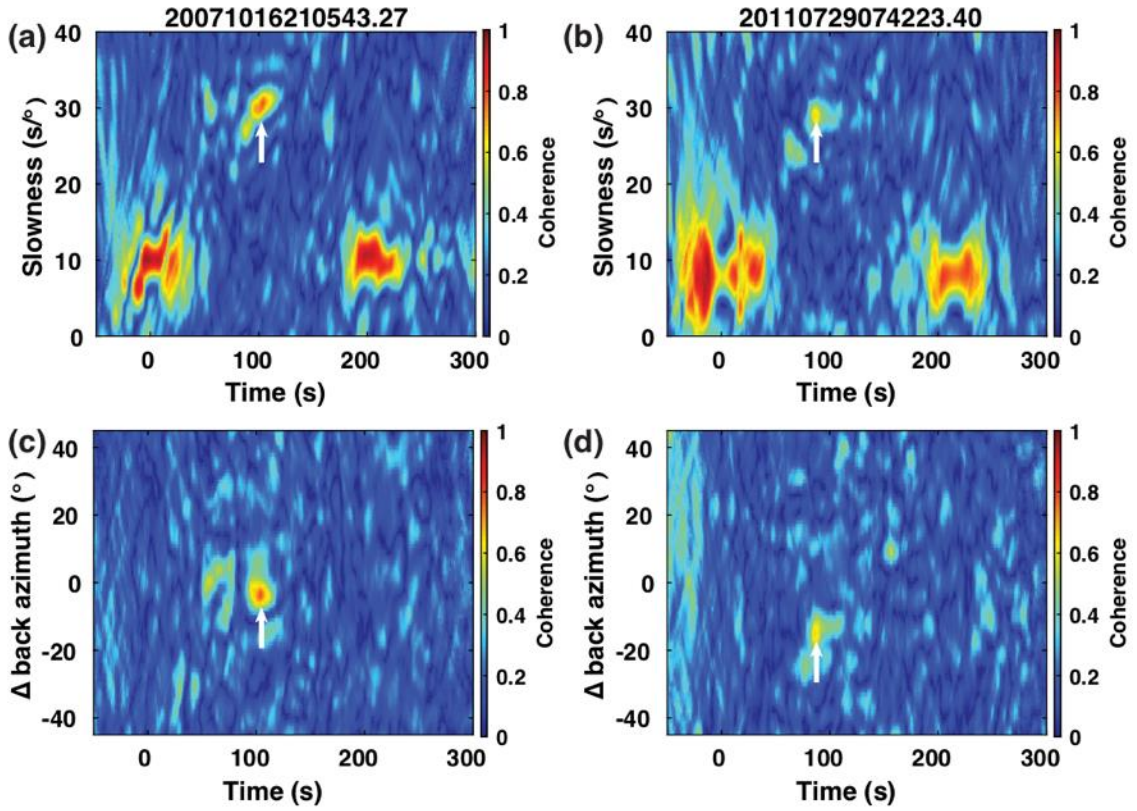

534

535 Figure 5 Coherence analyses of recorded seismic waveforms shown in Figure 4c,d. (a), (c) are for
536 stations in the western US; (b), (d) for stations in the central US. The slownesses and back azimuths
537 of scattered Love waves can be determined by picking up the maximum coherence in the expected
538 slowness window (marked by white arrows).

539

540

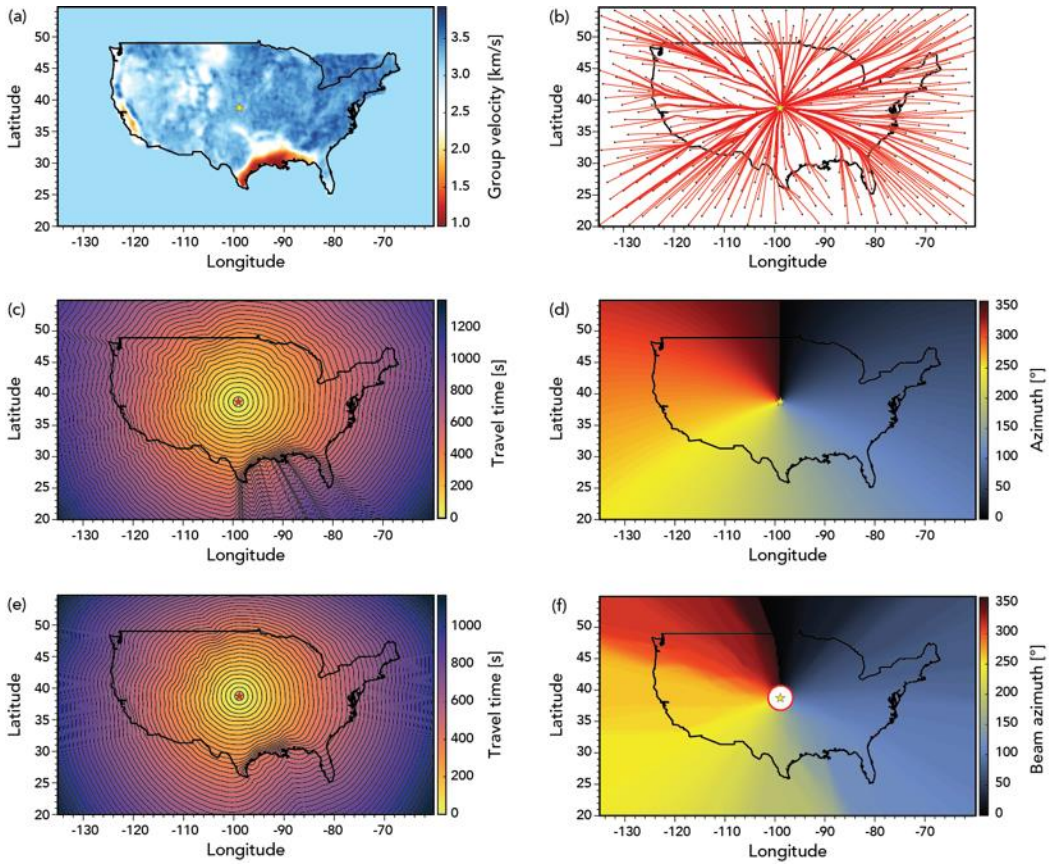

Figure 6 Love wave group velocity map and corresponding ray tracing. (a) 10 s Love-wave group velocity calculated from USANT15 (Ekström, 2017). (b) curved-ray tracing using the Eikonal solver for a hypothetical subarray center in the central US. (c) and (d) are distributions of travel times and back azimuths, respectively, for straight-ray tracing. (e) and (f) are the same as (c) and (d), but for curved-ray tracing. The red and yellow star in all panels mark the location of the hypothetical subarray center. The red circle in (f) depicts the 2°-radius subarray used to beamform the theoretical arrival times and extract the apparent back azimuths.

550

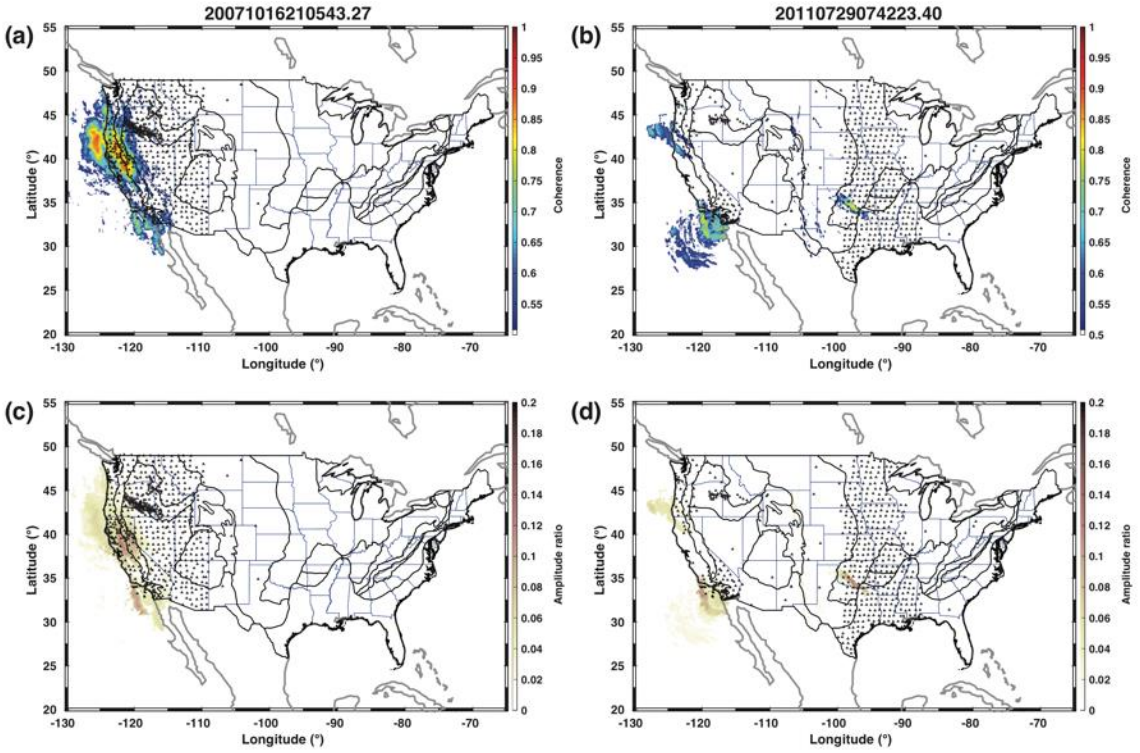

551

552 Figure 7 Straight-ray back-projection of scattered surface wave. The top panels (a) and (b) are for
553 phase coherence. The bottom panels (c) and (d) are for the envelop of stacked amplitude
554 (normalized by direct *SH* or *Sdiff* wave). Results for all subarrays are combined together. (a), (c) are
555 for the 2007 event. (b), (d) are for the 2011 event.

556

557

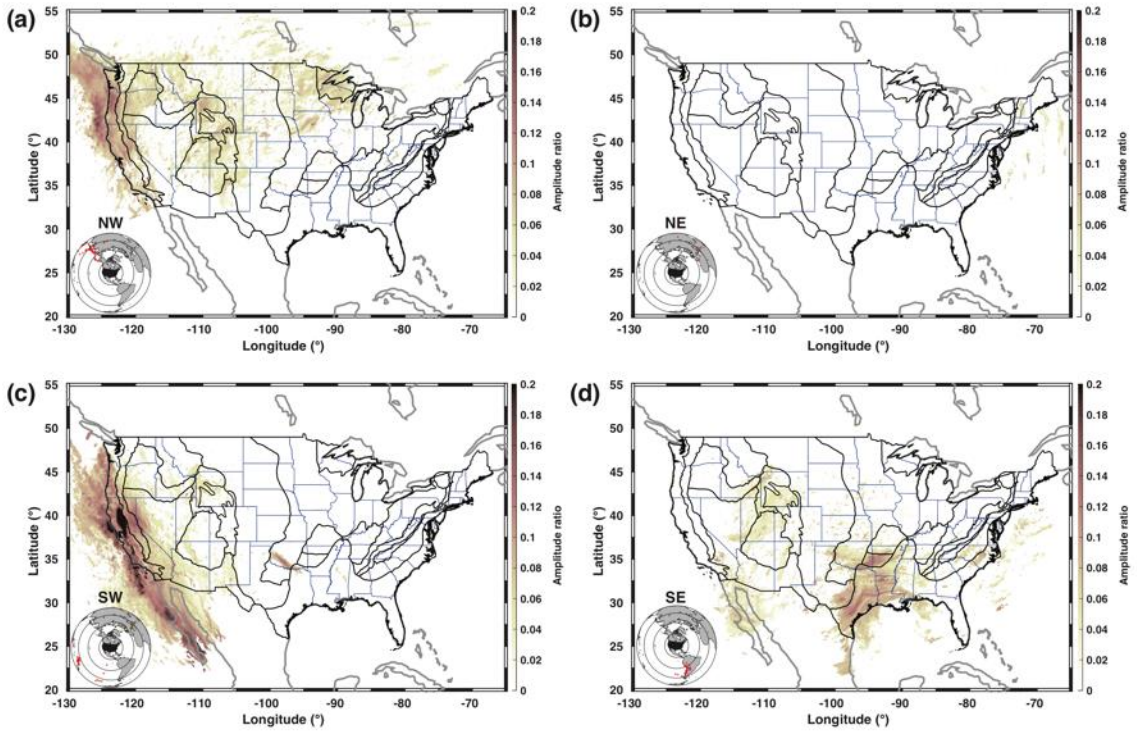

Figure 8 Directional sensitivity of scattering strength across the contiguous US. (a), (b), (c) and (d) are straight-ray back-projection results for events from NW, NE, SE and SW directions, respectively.

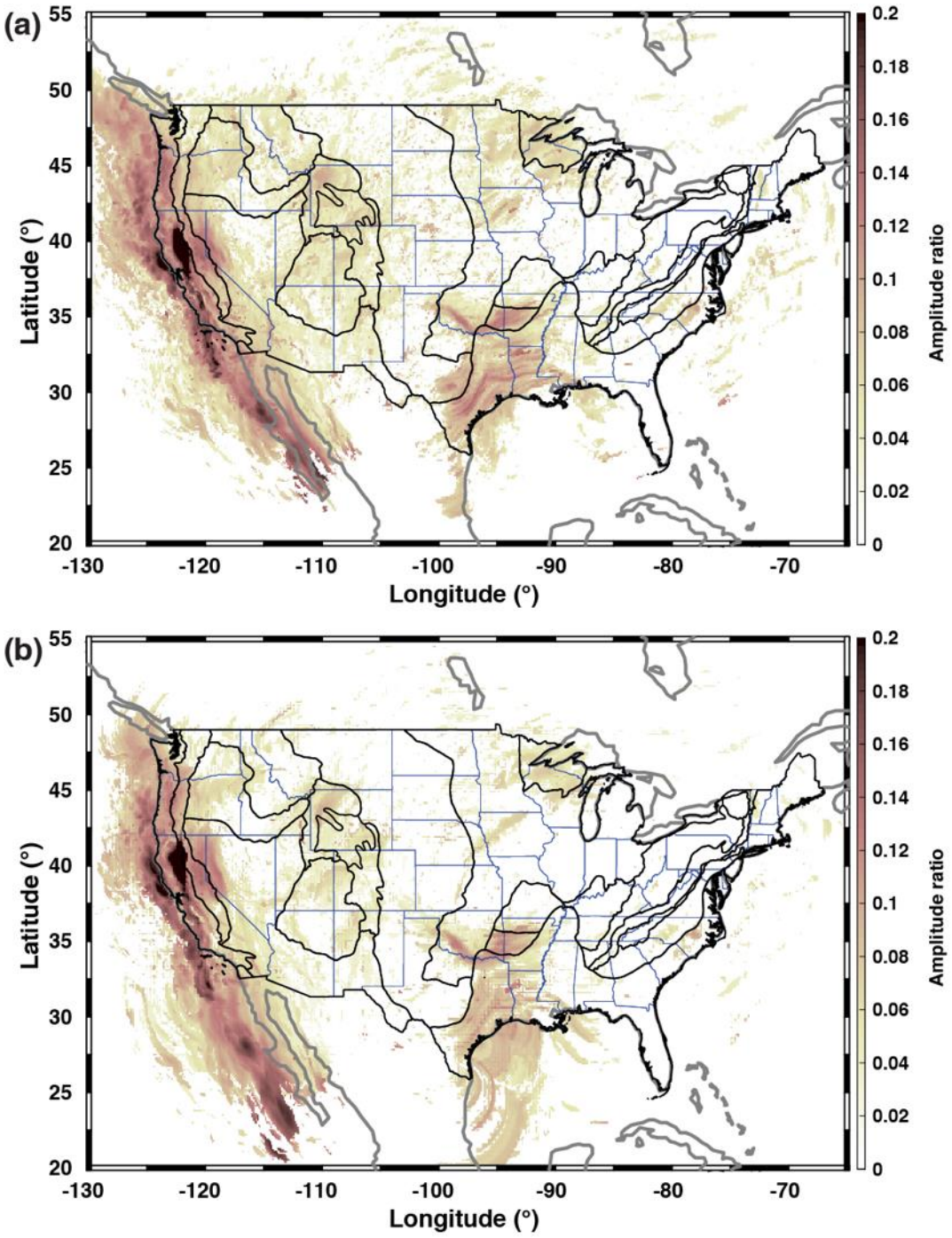

563

564 Figure 9 Composite back-projection results across the contiguous United States. (a) and (b) are for
565 straight-ray and curved-ray back-projections, respectively. Results for all events are merged
566 together.

567

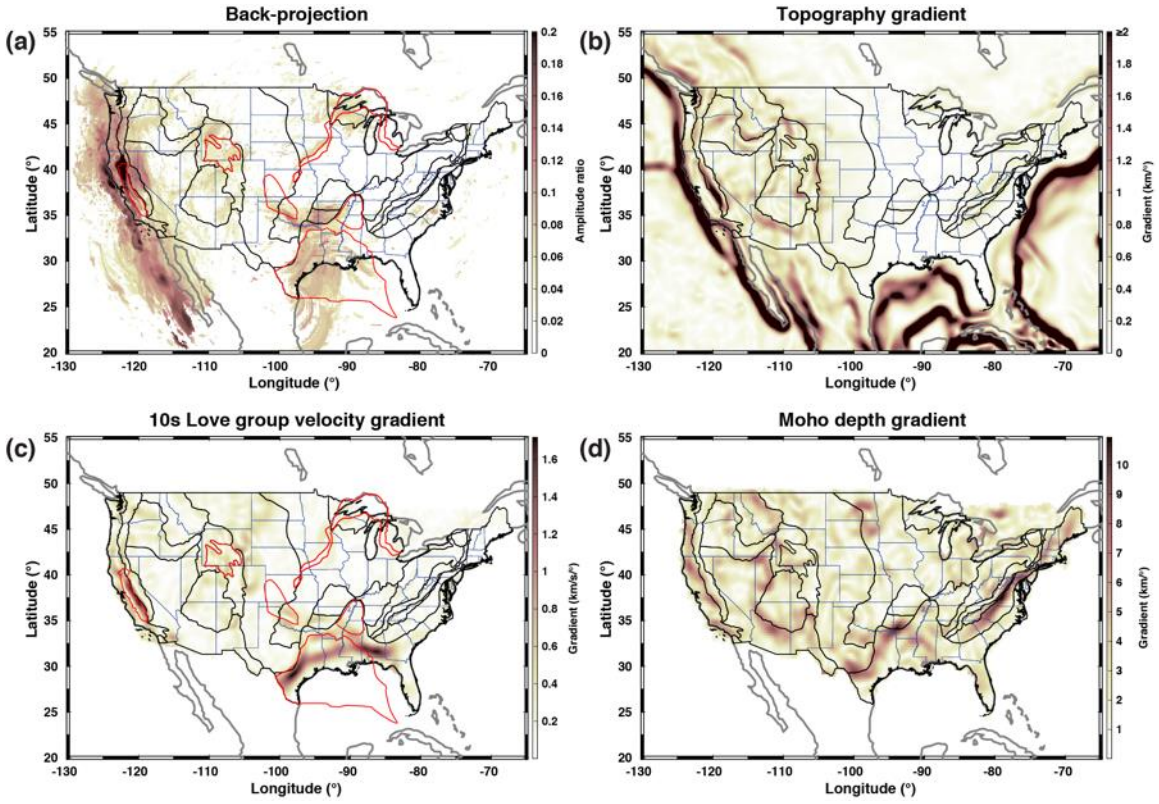

Figure 10 Comparison between curved-ray back-projection results with horizontal gradients of (sub)surface structures. (b), (c) and (d) are for topographic relief, 10s Love-wave group velocity, and Moho depth, respectively. A gaussian filter with a standard deviation of 1° in radius is applied to remove short-wavelength features.

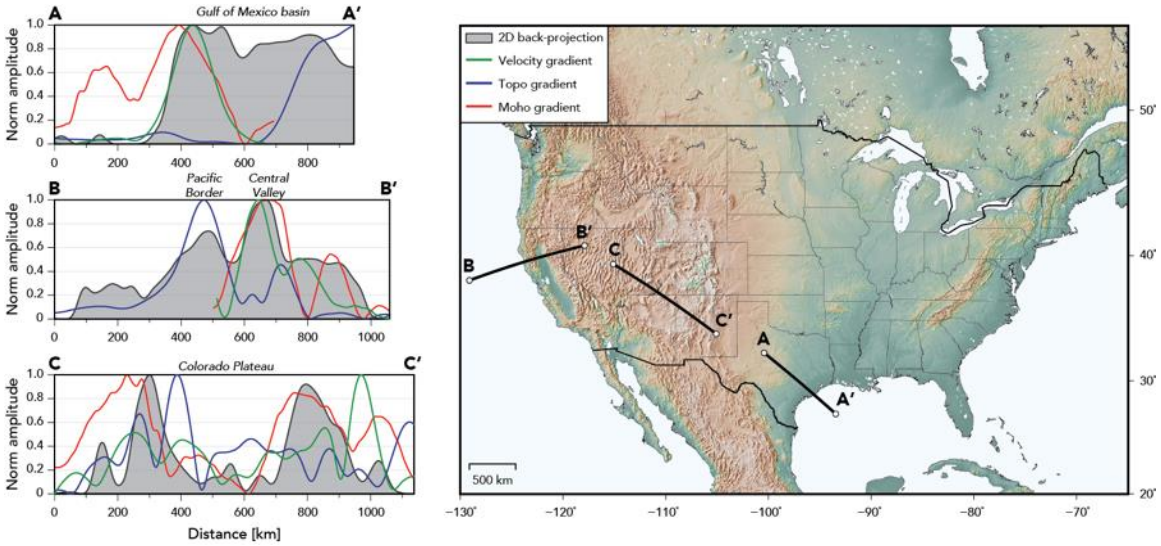

574

575 Figure 11 A detailed comparison of back-projection results (gray-filled curve) with horizontal
576 gradients of the 10s Love-wave group velocity (green curve), topography (blue curve) and Moho
577 depth (red curve) along three selected profiles.

578

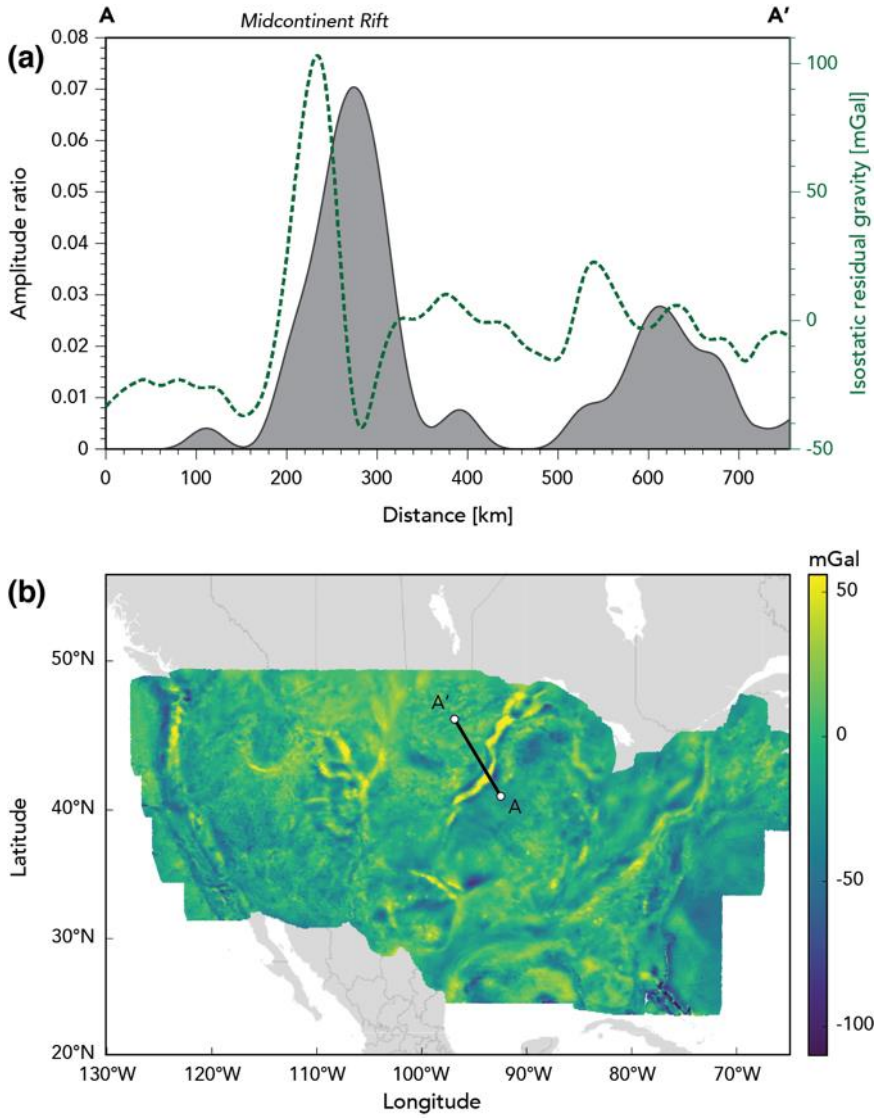

579

580 Figure 12 (a) Comparison between back-projection results (gray-filled curve) with the isostatic
581 residual gravity anomaly (Kucks, 1999) across the midcontinent rift zone (profile AA'). (b) Free-air
582 gravity anomaly map with location of the AA' profile.

583

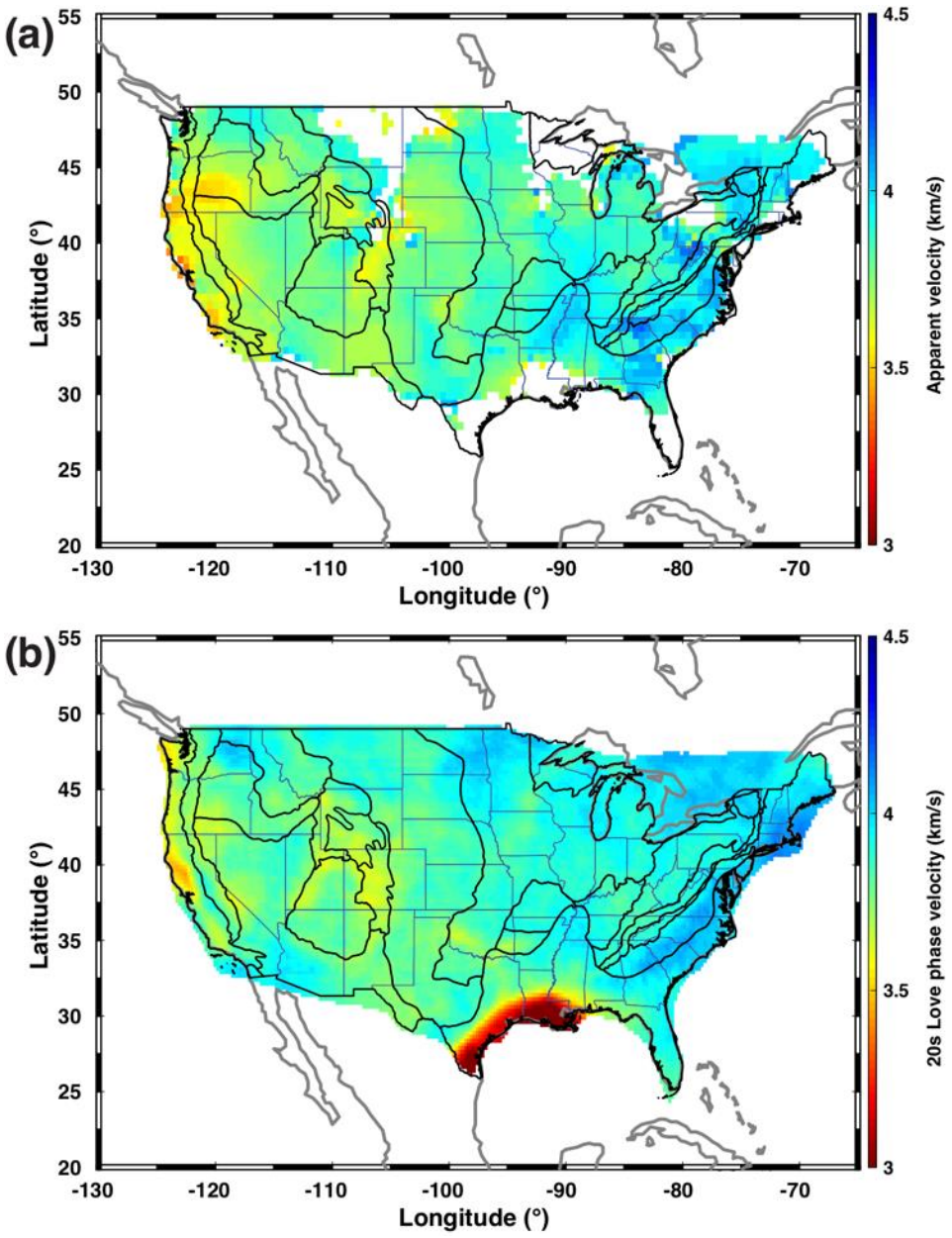

584

585 Figure 13 Comparison between (a) our estimated apparent velocity of scattered surface wave and
586 (b) 20s Love-wave phase velocity of USANT15 (Ekström, 2017). Note that the estimated apparent
587 velocity is averaged over a certain frequency range, which varies for different events and locations.

588